

Article

Temporal Solitons in an Optically Injected Kerr Cavity with Two Spectral Filters

Alexander Pimenov [†] and Andrei G. Vladimirov ^{*,†}

Weierstrass Institute, Mohrenstr. 39, 10117 Berlin, Germany

* Correspondence: andrei.vladimirov@wias-berlin.de

† These authors contributed equally to this work.

Abstract: We propose and analyze a theoretical scheme of an injected Kerr cavity, where the chromatic dispersion is induced by propagation of light through two Lorentzian spectral filters with different widths and central frequencies. We show that this setup can be modeled by a second order delay differential equation that can be considered as a generalization of the Ikeda map with included spectral filtering, dispersion, and coherent injection terms. We demonstrate that this equation can exhibit modulational instability and bright localized structures formation in the anomalous dispersion regime.

Keywords: temporal cavity solitons; Kerr cavity; chromatic dispersion; frequency combs

1. Introduction

Optical frequency combs generated from a continuous wave laser output in micro-cavity Kerr resonators have revolutionized many fields of natural science and technology [1]. Of particular interest are the so-called soliton frequency combs [2–4] associated with the formation in the time domain of the temporal cavity solitons—nonlinear localized structures of light, which preserve their shape in the course of propagation [5]. Kerr cavity temporal dissipative solitons were reported experimentally in micro-cavity resonators [2,6–8], and in driven fiber cavities [9]. Spectral filtering is commonly used to improve the output characteristics of multisection mode-locked lasers [10]. It was also demonstrated that a small spectral filtering can suppress the oscillatory instability of Kerr cavity solitons and stabilize their bound states by eliminating high frequency perturbations [11–14]. On the other hand, unlike conventional Kerr cavities, where spectral filtering is only a small perturbation, in Mamyshev oscillators a pair of spectral filters plays a crucial role in the process of the short pulse generation [15,16]. The nonlinear dynamics of such two filter systems is yet to be understood theoretically. In order to fill this gap we consider an externally driven Kerr cavity with two spectral filters and demonstrate that the effective dispersion created by the filters can lead to a temporal soliton generation even when the material dispersion is negligibly small.

Time-delay models of optical systems like Ikeda map [17], Lang-Kobayashi equations [18], delay differential equation (DDE) mode-locked laser models [19–27], frequency swept laser models [28,29], and others were successfully used to describe unidirectional propagation of light through linear and nonlinear optical elements in a ring cavity. Unlike simple complex Ginzburg-Landau (CGL)-type models of passive and active optical cavities based on the mean field approximation, these models are valid for arbitrary large gain and losses in the cavity. An important drawback of the time-delay models, however, is that the inclusion of an arbitrary second order chromatic dispersion of the intracavity media into these models is not a trivial task. Recently, it was shown that chromatic dispersion in photonic crystal mode-locked laser [30] and a SOA-fiber laser with fiber delay line [31] can be described using a distributed delay term, which arises from the transfer function of a



Citation: Pimenov, A.; Vladimirov, A.G. Temporal Solitons in an Optically Injected Kerr Cavity with Two Spectral Filters. *Optics* **2022**, *3*, 364–383. <https://doi.org/10.3390/opt3040032>

Academic Editor: Thomas Seeger

Received: 29 August 2022

Accepted: 19 September 2022

Published: 23 September 2022

Publisher's Note: MDPI stays neutral with regard to jurisdictional claims in published maps and institutional affiliations.



Copyright: © 2022 by the authors. Licensee MDPI, Basel, Switzerland. This article is an open access article distributed under the terms and conditions of the Creative Commons Attribution (CC BY) license (<https://creativecommons.org/licenses/by/4.0/>).

detuned Lorentzian absorption line in frequency domain. Furthermore, under assumption of weak dispersion one can replace the distributed time delay model with an extended DDE model containing a single additional ordinary differential equation for the polarization variable [32]. Using this extended DDE model, the conventional combined effects of chromatic dispersion and nonlinearity such as modulational instability (MI) in the anomalous dispersion regime and bright localized structures formation were demonstrated [32]. Nevertheless, these assumptions and approximations limit our ability to describe accurately and characterize chromatic dispersion at all the frequencies that are important for dynamics of optical devices using DDE models. Another approach is to investigate rigorously derived DDEs where higher order dispersion arises naturally (e.g., coupled cavities [33]), however quantification of its magnitude for a given DDE is not a trivial task.

In this paper, we consider an externally injected ring Kerr cavity with two linear spectral filters introducing an effective chromatic dispersion and demonstrate the possibility to model arbitrary second-order dispersion near a chosen frequency within the DDE framework. We develop a second order DDE model of the system under consideration and demonstrate the appearance of MI and the formation of bright localized structures in this model in the anomalous dispersion regime. The system under consideration can be realized experimentally to generate temporal cavity solitons and the corresponding optical frequency combs [6,34]. We show that in a certain limit our model can be reduced to a generalized version of the well-known Lugiato-Lefever equation [35], which is widely used to describe optical microcomb generation [36–38], with an additional diffusion term. These results can be applied to qualitatively analyze any optical set-up that can be modeled using delay equations such as Fourier domain mode-locked [31], optically injected [32], and multisection mode-locked semiconductor lasers as well as any other system, where second-order chromatic dispersion is important (see references in [31]). We note also that two spectral filters with different central frequencies are used in Mamyshev oscillators, which employ active cavity to generate short optical pulses. Hence, this work not only presents the simplest dispersive second-order DDE model that can describe complicated phenomena like localized structures, but also could provide better understanding of the effect of two filters in the cavity and a basis for the theoretical investigation of Mamyshev oscillators [15,16].

2. Model Equations

We consider an optically injected passive nonlinear cavity with two linear Lorentzian filters inside it (see Figure 1). For this system using the lumped element method described in [19–21] we obtain the following set of delay differential equations

$$B'(t) + (\gamma_1 - i\omega_1)B(t) = \gamma_1\gamma_2 \left[\sqrt{\kappa_l} e^{i\alpha|A(t-T)|^2 + i\varphi} A(t-T) + \eta_0 e^{i\omega_0 t} \right], \quad (1)$$

$$A'(t) + (\gamma_2 - i\omega_2)A(t) = B(t), \quad (2)$$

where B and A represent electrical field envelopes after the first and the second filter, respectively, T is the cavity round-trip time, κ_l is the intensity attenuation factor due to the linear cavity losses, φ is the phase shift, α is the Kerr coefficient which, without the loss of generality can be assumed to be positive, η_0 and ω_0 are the injection rate and frequency offset, ω_1 and ω_2 are the central frequencies of the two filters, while γ_1 and γ_2 are their bandwidths. The system (1) and (2) can be considered as an extension of the Ikeda map [17], which takes into consideration the spectral filtering introduced by two Lorentzian filters.

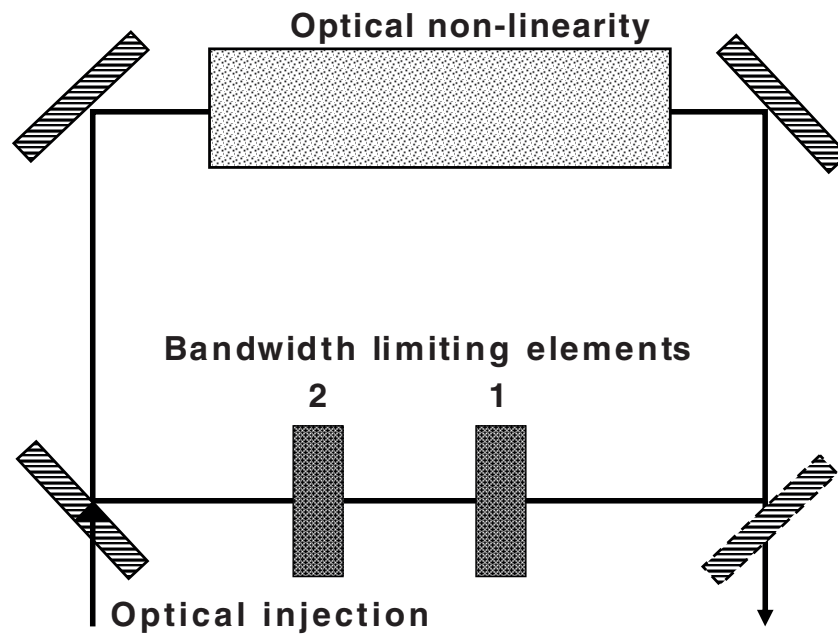


Figure 1. Schematic representation of the considered device.

2.1. Transfer Function of the Filter

The transfer function of the two filters shown in Figure 1 can be written in the standard form [30,31]

$$F(\omega) = e^{f(\omega)}, \tag{3}$$

where the complex function $f(\omega)$ can be expanded in power series near $\omega = 0$

$$f(\omega) = \sum_k D_k \omega^k, \tag{4}$$

and $\Im D_k$ represents the dispersion of the k th order. (For example, for a single Lorentzian absorption line we have $f = \frac{-\sigma L}{\Gamma + i(\omega + \Omega)}$ [31], and second-order dispersion coefficient takes the form $\Im D_2 = \Im \frac{d^2 f}{d\omega^2} \approx \frac{2\sigma L}{\Omega^3}$ for $0 < \Gamma \ll |\Omega|$, and the sign of the coefficient coincides with the sign of Ω .)

From Equations (1) and (2) one obtains that the two filter transfer function is

$$F(\omega) = \frac{\gamma_1 \gamma_2}{[\gamma_1 + i(\omega - \omega_1)][\gamma_2 + i(\omega - \omega_2)]}. \tag{5}$$

Since in the frequency domain the transfer functions of two filters are multiplied, see Equation (5), their ordering does not play any role. Therefore, without loss of generality we can assume that $\gamma_1 \geq \gamma_2$ and the reference frequency is chosen in such a way that the maximum of the function $|F(\omega)|$ is at $\omega = 0$, so that $\left[\frac{d|F(\omega)|}{d\omega} \right]_{\omega=0} = 0$. The latter condition is equivalent to

$$\delta_F = \gamma_2^2 \omega_1 + \omega_2 [\gamma_1^2 + \omega_1(\omega_1 + \omega_2)] = 0, \tag{6}$$

which has two solutions $\omega_2 = \omega_{2\pm} = \frac{-\gamma_1^2 - \omega_1^2 \pm \sqrt{D_F}}{2\omega_1}$, $D_F = -4\gamma_2^2 \omega_1^2 + (\gamma_1^2 + \omega_1^2)^2$. One can see that both $\omega_{2\pm}$ can be obtained for any values of $\omega_1 \neq 0$ and $0 < \gamma_2 < \gamma_1$ due to $D_F > 0$, and, moreover,

$$|\omega_1^2 - \gamma_1^2| \leq \sqrt{D_F} \leq \gamma_1^2 + \omega_1^2.$$

Below we will assume that the condition $\omega_2 = \omega_{2+}$ is satisfied that corresponds to a situation when the largest of the two maximums of $|F(\omega)|$ is located at zero frequency, see Figure 2. In the left panel of this figure we fix $\gamma_1 = \gamma_2 = 1$ and demonstrate that for

$\omega_1 < 1$ we have one global maximum, whereas for $\omega_1 > 1$ we can get two local maxima in our combined filter of the same magnitude. In the second case, or for values of γ_2 close to γ_1 , this kind of filter can lead to complex dynamical behaviour in the system, similarly to the case of the Mamyshev oscillator [15,16]. However, in this paper we are focused on the impact of the filter on the frequency of injection, which is assumed to be near or at the global maximum at zero frequency. In the right panel we can observe how the second maximum is suppressed with γ_2 decreasing from 1 to $\frac{1}{8}$. For $\omega_2 = \omega_{2+}$ we have

$$\omega_2\omega_1 < 0, \quad |\omega_2| \leq |\omega_1|, \quad \left| \frac{d\omega_2}{d\omega_1} \right| < 1,$$

and one can see that

$$\frac{d|\omega_2 - \omega_1|}{d|\omega_1|} > 0,$$

i.e., the difference between the two frequencies grows with $|\omega_1|$, and since for any of $\omega_1 = \pm\omega_1^*$ we have $\omega_2 = \mp\omega_2^*$, respectively, for any fixed $0 < \gamma_2 < \gamma_1$ we can choose $|\omega_2 - \omega_1|$ and find corresponding value of ω_1 (negative or positive) and $\omega_2 = \omega_{2+}$, which means that we can have any possible combinations of two filters (narrow filter to the left or to the right of the broad filter), disregarding frequency shift of the combined filter. Moreover, these inequalities immediately imply that the largest maximum of $|F(\omega)|$ is at $\omega = 0$ for $\omega_2 = \omega_{2+}$ as claimed earlier, since more narrow Lorentzian filter with the width γ_2 has the central frequency ω_2 closer to zero frequency. The other root (6) $\omega_2 = \omega_{2-}$ can correspond to a global maximum, a local maximum, or a local minimum, which do not provide any additional useful alternatives, if we are interested to fix the maximum of the combined filter $|F(\omega)|$ at zero frequency $\omega = 0$.

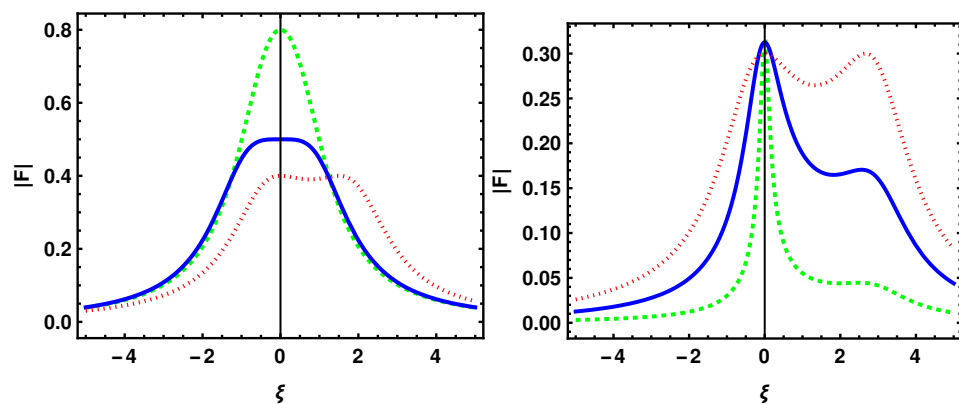


Figure 2. Absolute value of the transfer function F defined by Equation (5), where $\omega_2 = \omega_{2+}$ satisfies (6), $\gamma_1 = 1$ and other parameters are varied: (left) $\gamma_2 = 1, \omega_1 = \frac{1}{2}$ (dashed), $\omega_1 = 1$ (solid), $\omega_1 = 2$ (dotted); (right) $\omega_1 = 3, \gamma_2 = \frac{1}{8}$ (dashed), $\gamma_2 = \frac{1}{2}$ (solid), $\gamma_2 = 1$ (dotted). The corresponding values of ω_2, β, σ are $\{-\frac{1}{2}, -1, -\frac{1}{2}\}, \{0, 0, \frac{3}{4}\}$ and $\{\frac{4}{\sqrt{5}}, \sqrt{2}, \frac{5}{\sqrt{8}}\}$ (left); $\{-0.0047, -0.07677, -\frac{1}{3}\}, \{2.66, 1.95, \frac{4}{3}\}$ and $\{8.58, 3.84, \frac{5\sqrt{2}}{3}\}$ (right).

Since $f(\omega) = \ln F(\omega)$, in the power series expansion (4) we obtain the second-order coefficient as

$$D_2 = \frac{\omega_1^2 - \gamma_1^2 - 2i\gamma_1\omega_1}{2(\gamma_1^2 + \omega_1^2)^2} + \frac{\omega_2^2 - \gamma_2^2 - 2i\gamma_2\omega_2}{2(\gamma_2^2 + \omega_2^2)^2}.$$

One can check that D_2 can be represented in the following way

$$D_2 = \rho \left(-\frac{\sigma^2 - 2}{2} + i\beta \right) + \frac{\delta_F [\delta_F - 2i(\gamma_1^2\gamma_2 + \gamma_1\gamma_2^2 + \gamma_2\omega_1^2 + \gamma_1\omega_2^2)]}{2(\gamma_1^2 + \omega_1^2)(\gamma_2^2 + \omega_2^2)(\gamma_1\gamma_2 - \omega_1\omega_2)}, \quad (7)$$

with

$$\rho = \frac{\gamma_1 \gamma_2 - \omega_1 \omega_2}{(\gamma_1^2 + \omega_1^2)(\gamma_2^2 + \omega_2^2)}, \tag{8}$$

$$\sigma = \frac{\sqrt{\rho}(\gamma_1^2 \gamma_2 + \gamma_1 \gamma_2^2 + \gamma_2 \omega_1^2 + \gamma_1 \omega_2^2)}{\gamma_1 \gamma_2 - \omega_1 \omega_2}, \tag{9}$$

$$\beta = \frac{\gamma_1 \omega_2 + \gamma_2 \omega_1}{\gamma_1 \gamma_2 - \omega_1 \omega_2}. \tag{10}$$

It follows from the conditions (6), where $\omega_2 = \omega_{2+}$, and the relation $\gamma_1 \geq \gamma_2$ that the second term in the right hand side (RHS) of (7) vanishes, $\rho > 0$, and $\text{sign}\beta = \text{sign}\omega_1$. Hence, the parameters β and $\frac{\sigma^2 - 2}{2}$ represent the normalized second-order dispersion and the diffusion near zero frequency, respectively, whereas the parameter $\sqrt{\rho}$ can be considered as a scaling coefficient.

One can see that under these conditions

$$\frac{d|\beta|}{d|\omega_1|} > \frac{\sqrt{D}(\sqrt{D} + \omega_1^2 - \gamma_1^2)}{4\gamma_1\omega_1^2(\gamma_1^2 + \omega_1^2)} > 0,$$

and since $|\omega_2 - \omega_1|$ grows with $|\omega_1|$, second-order dispersion grows with the difference between the frequencies. Moreover, using (6) to express ω_2^2 one obtains

$$\begin{aligned} \sigma &= \frac{(\gamma_2 \omega_1 - \gamma_1 \omega_2) \text{Sign } \omega_1}{\sqrt{\omega_1 \omega_2 (\omega_1 \omega_2 - \gamma_1 \gamma_2)}}, \\ \frac{d\sigma}{d\gamma_2} &= \frac{|\omega_1|(\gamma_1 \gamma_2 \omega_1 + (\gamma_1^2 - 2\omega_1^2)\omega_2)(\gamma_2 \frac{d\omega_2}{d\gamma_2} - \omega_2)}{2(\omega_1 \omega_2 (\omega_1 \omega_2 - \gamma_1 \gamma_2))^{3/2}}, \\ \gamma_2 \frac{d\omega_2}{d\gamma_2} - \omega_2 &= \omega_2 \frac{\gamma_1^2 + \omega_1^2}{2\sqrt{D}}, \\ \omega_1(\gamma_1 \gamma_2 \omega_1 + (\gamma_1^2 - 2\omega_1^2)\omega_2) &< -\frac{\gamma_1^2(\gamma_1^2 + \omega_1^2)}{2}, \end{aligned}$$

hence due to $\omega_1 \omega_2 < 0$ we see that $\frac{d\sigma}{d\gamma_2} < 0$, and σ decreases with γ_2 increasing from 0 to γ_1 . Therefore, the lower bound on σ can be estimated assuming $\gamma_2 = \gamma_1$, where $\omega_2 = \frac{-\gamma_1^2 - \omega_1^2 + |\omega_1^2 - \gamma_1^2|}{2\omega_1}$ and

$$\sigma \geq \sigma_{\gamma_2=\gamma_1} = \begin{cases} \sqrt{2}\sqrt{1+\beta^2}, & |\omega_1| \geq \gamma_1, \\ 2\frac{\gamma_1\sqrt{1+\beta^2}}{\sqrt{\gamma_1^2+\omega_1^2}}, & |\omega_1| < \gamma_1. \end{cases} \geq \sqrt{2}\sqrt{1+\beta^2}. \tag{11}$$

2.2. Normalized DDE Model

By substituting Equation (2) into Equation (1), using Equation (6), and rescaling time as $t \rightarrow t/\sqrt{\rho}$, we obtain the following normalized dimensionless second-order DDE

$$\begin{aligned} A''(t)(1+i\beta) + \sigma A'(t) + A(t) &= \sqrt{\kappa} e^{i\alpha|A(t-T)|^2 + i\varphi} A(t-T) + \eta e^{i\omega_0 t}, \\ \sigma &> \sqrt{2}\sqrt{1+\beta^2}, \end{aligned} \tag{12}$$

where losses and forcing take the form $\sqrt{\kappa} = r\sqrt{\kappa_l} \leq 1, \eta = r\eta_0$ with $r = \frac{\gamma_1 \gamma_2}{\sqrt{(\gamma_1^2 + \omega_1^2)(\gamma_2^2 + \omega_2^2)}} \leq 1$, and the phase shift is $\varphi = \phi + \arg \frac{1}{\gamma_2 \gamma_2 - \omega_1 \omega_2 - i(\gamma_1 \omega_2 + \omega_2 \gamma_1)}$. Here, similarly to the previous section one can see that $\frac{dr}{d|\omega_1|} < 0$ for $\gamma_1 > \gamma_2$ and $\omega_2 = \omega_{2+}$, hence for fixed κ_l the parameter κ decreases with increasing detuning between the two frequencies $|\omega_2 - \omega_1|$. With the condition (11) on dimensionless parameters σ and β the equation is equivalent to the system with two filters (1) and (2) for any $\kappa < 1$ with global maximum of the combined

filter transfer function $F(\omega)$ (5) located at zero frequency $\omega = 0$, $|F(\omega)| \leq |F(0)| \leq 1$. We note that for $\sqrt{2} \leq \sigma \leq \sqrt{2(1 + \beta^2)}$ the global maximum of $F(\omega)$ is at another frequency and additional constraints on parameter κ are necessary, whereas for $\sigma < \sqrt{2}$ the diffusion coefficient in (7) becomes negative, equivalence with (1) and (2) is lost and zero solution $A = 0$ for $\eta = 0$ is unstable.

For $\beta = 0$ relation (7) gives zero dispersion coefficient and diffusion coefficient equal to $(\sigma^2 - 2)/2$, which agrees with previous analysis of a similar DDE [39] in case of $\sigma > \sqrt{2}$.

We note that the direct application of truncated expansion (4) in the RHS of DDE models similar to (1) and (12) would lead to the appearance of the second derivative of the delayed variable $A''(t - T)$ in and spurious instability [31]. In contrast, non-delayed second order derivative $A''(t)$ in (12) appears without any expansions, and the term $i\beta A''(t)$ is responsible for the second-order chromatic dispersion similarly to the CGL equations. On the other hand, unlike the cubic CGL model, where the real coefficient by the second derivative is responsible for the diffusion (or parabolic spectral filtering), the filtering in (12) is performed by two Lorentzian filters, which are introduced by the presence of both the first and the second order derivatives. Therefore, the generality of this kind of dispersion operator is still not directly comparable to the operators in CGL-type equations or systems with distributed delay [31]. However, in contrast to the approximate DDEs [32], the physical meaning of this filter is clear for any feasible parameters. For simplicity below we consider the case of non-detuned injection, $\omega_0 = 0$.

2.3. Limit of Lugiato-Lefever Equation

Assuming large delay limit $T = r/\epsilon$, where $\epsilon \ll 1$ and $r = 1 + a_1\epsilon + a_2\epsilon^2 + \dots$, taking $\omega_0 = 0$, and rescaling the time variable $t \rightarrow t/\epsilon$ we can rewrite (12) in the form

$$\epsilon^2 A''(t)(1 + i\beta) + \epsilon \sigma A'(t) + A(t) = \sqrt{\kappa} e^{i\alpha|A(t-r)|^2 + i\varphi} A(t-r) + \eta, \tag{13}$$

Let the injection rate, the linear cavity losses and the phase shift be small,

$$\eta = \epsilon^3 S, \quad \kappa = 1 - 2\epsilon^2 k, \quad \varphi = \epsilon^2 \theta. \tag{14}$$

Then looking the solution in the form $A(t) = \epsilon u(t, \tau) + \epsilon^2 v(t, \tau) + \dots$ with $\tau = \epsilon^2 t$, applying multiscale analysis [40,41], collecting the first order in ϵ , and using solvability condition of the resulting equation we get the periodic boundary condition:

$$u(t, \tau) = u(t - 1, \tau). \tag{15}$$

Next, in the second order in ϵ we obtain

$$v(t, \tau) - v(t - 1, \tau) = a_1 u_t(t - 1, \tau) - \sigma u_t(t, \tau),$$

which implies the periodicity of v , $v(t - 1, \tau) = v(t, \tau)$ and the relation $a_1 = \sigma$ with the periodicity condition (15). Finally collecting the third order terms in ϵ , using the relation $a_2 = \sigma^2$, and applying solvability condition [40,41] we get the generalized Lugiato-Lefever equation (LLE)

$$u_\tau = S - ku + i\theta u + i\alpha u|u|^2 + \left(\frac{\sigma^2 - 2}{2} - i\beta \right) u_{tt} \tag{16}$$

with the diffusion coefficient $(\sigma^2 - 2)/2$ and the boundary condition (15). It is well known that for $\beta < 0$ in Equation (16) corresponds to anomalous dispersion regime, and for $\theta < 0$ this equation can demonstrate the formation of bright dissipative solitons [35]. Dimensionless dispersion and diffusion coefficients in Equation (16) coincide with those defined by Equation (7).

3. Continuous Wave (CW) State

The CW state of the Equation (12) with $\omega_0 = 0$ takes the form $A = A_0 e^{i\psi}$, where the real quantities A_0 and ψ satisfy the system of the transcendental equations

$$A_0 \left[1 - \sqrt{\kappa} \cos(\alpha A_0^2 + \varphi) \right] = \eta \cos \psi, \tag{17}$$

$$A_0 \sqrt{\kappa} \sin(\alpha A_0^2 + \varphi) = \eta \sin \psi, \tag{18}$$

which leads to a single transcendental equation for A_0^2

$$A_0^2 \left[\kappa + 1 - 2\sqrt{\kappa} \cos(\alpha A_0^2 + \varphi) \right] = \eta^2. \tag{19}$$

Assuming $\varepsilon \ll 1$, $A_0 = \varepsilon u_0$, $\varphi = \varepsilon^2 \theta$, $0 < 1 - \kappa \sim 2\varepsilon^2 k$, and $\eta = \varepsilon^3 S$, this equation can be approximated by a cubic equation for u_0^2

$$S^2 \approx u_0^2 \left[k^2 + (\theta + \alpha u_0^2)^2 \right], \tag{20}$$

which coincides with the equation for the uniform stationary solutions of the LLE (16). Therefore, in this limit Equation (12) can have up to three coexisting CW states similarly to LLE (see Figure 3, left), however out of this limit for strong injection there can be more coexisting CW states, see right panel of Figure 3. Here, the upper CW state loses stability via a modulational instability, and unstable CW states are shown by dotted red line.

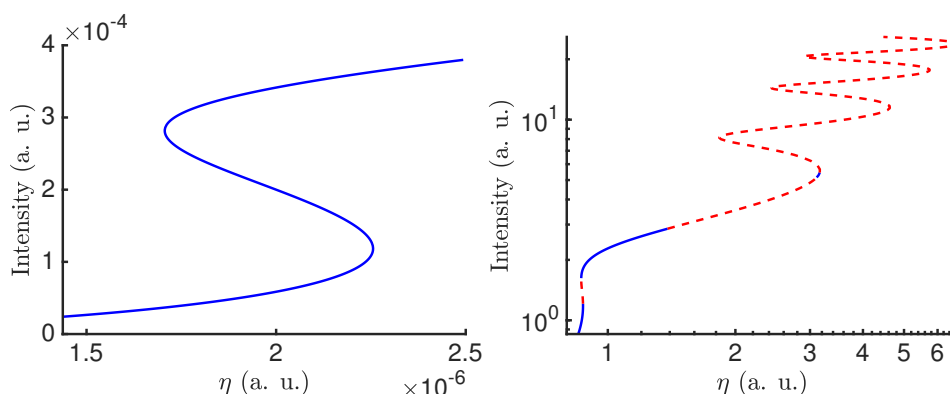


Figure 3. Intensity $|A_0|^2$ of CW states (17) and (18) obtained by varying parameter η (left). Here, $\omega_0 = 0$, $\kappa = 1 - 10^{-4}$, $\sigma = \sqrt{2.5}$, $\alpha = 1$, $\varphi = -3 \times 10^{-4}$, which in the LLE limit (13) corresponds to $\varepsilon = 0.01$. In the right panel we choose $\kappa = \exp(-2)$, $\varphi = -2$, which corresponds to $\varepsilon = 1$, where solid lines correspond to stable CWs and dashed - to unstable.

Stability of CW Solution and MI

Here, we demonstrate how MI of an initially stable CW state can appear in the anomalous dispersion regime in the limit of large delay $T \gg 1$. For that, we linearize the Equation (12) near the CW state $A(t) = (A_0 + \delta A e^{\lambda t}) e^{i\psi}$ and calculate the determinant of the Jacobian of the linearised system to obtain the following characteristic equation for the eigenvalues λ describing the stability of the CW solution:

$$\begin{aligned} & \kappa Y^2 + \lambda \{ \lambda [(\beta^2 + 1) \lambda^2 + 2\lambda\sigma + \sigma^2 + 2] + 2\sigma \} + 1 + \\ & 2\sqrt{\kappa} Y \{ \sin(\alpha A_0^2 + \varphi) [\alpha A_0^2 (\lambda^2 + \lambda\sigma + 1) - \beta \lambda^2] - \\ & \cos(\alpha A_0^2 + \varphi) [\lambda^2 (\alpha A_0^2 \beta + 1) + \lambda\sigma + 1] \} = 0. \end{aligned} \tag{21}$$

where $Y(\lambda) = \exp(-\lambda T)$. In the limit of large delay time $T \rightarrow \infty$ the eigenvalues belonging to the pseudo-continuous spectrum can be represented in the form $\lambda = i\mu + \frac{\Lambda}{T} + \mathcal{O}(1/T^2)$

with real μ [42]. Thus, in this limit the characteristic equation is a quadratic equation for Y with the coefficients depending only on the imaginary part μ of the eigenvalue, and we can obtain from (21) two branches of pseudo-continuous spectrum given by

$$\Lambda_{\pm}(\mu) = -\Re \ln Y_{\pm}(i\mu). \tag{22}$$

For a stable CW solution we have $\Lambda_{\pm}(\mu) \leq 0$ and, in particular, $\Lambda_{\pm}(0) = -\Re \ln Y_{\pm}(0) \leq 0$, where

$$Y_{\pm}(0) = \frac{1}{\sqrt{\kappa}} \left[\cos(\alpha A_0^2 + \varphi) - \alpha A_0^2 \sin(\alpha A_0^2 + \varphi) \pm \sqrt{D} \right], \tag{23}$$

$$D = \left[\cos(\alpha A_0^2 + \varphi) - \alpha A_0^2 \sin(\alpha A_0^2 + \varphi) \right]^2 - 1. \tag{24}$$

Moreover, the second derivative of $\Lambda_{\pm}(\mu)$ at $\mu = 0$ takes the form

$$\Lambda_{\pm}''(0) = 2 - \sigma^2 \pm 2\beta \Re \mathcal{B}(\alpha, \varphi, \eta, \kappa), \tag{25}$$

$$\mathcal{B} = \frac{\alpha A_0^2 \cos(\alpha A_0^2 + \varphi) + \sin(\alpha A_0^2 + \varphi)}{\sqrt{D}}. \tag{26}$$

One can see from (25) that for small $\beta \approx 0$ and $\sigma > \sqrt{2}$ we have $\Lambda_{\pm}''(0) < 0$ for the CW solutions on the upper branch of S-shaped bifurcation curve depicted in Figure 3 (see top-left panel of Figure 4). It is known that strong anomalous dispersion can lead to the change of the curvature of one of the two branches $\Lambda_{\pm}(\mu)$ of the pseudo-continuous spectrum at $\mu = 0$ (see Figure 4, bottom-left) [31]. Moreover, further increase of anomalous dispersion can lead to a MI of a CW state (see Figure 4, bottom-right) [32]. On the other hand, in the case of strong normal dispersion regime the sign change of the curvature of the curve with smaller $\Lambda_{\pm}(0)$ does not lead to a MI, as it is seen from the top-right panel of Figure 4.

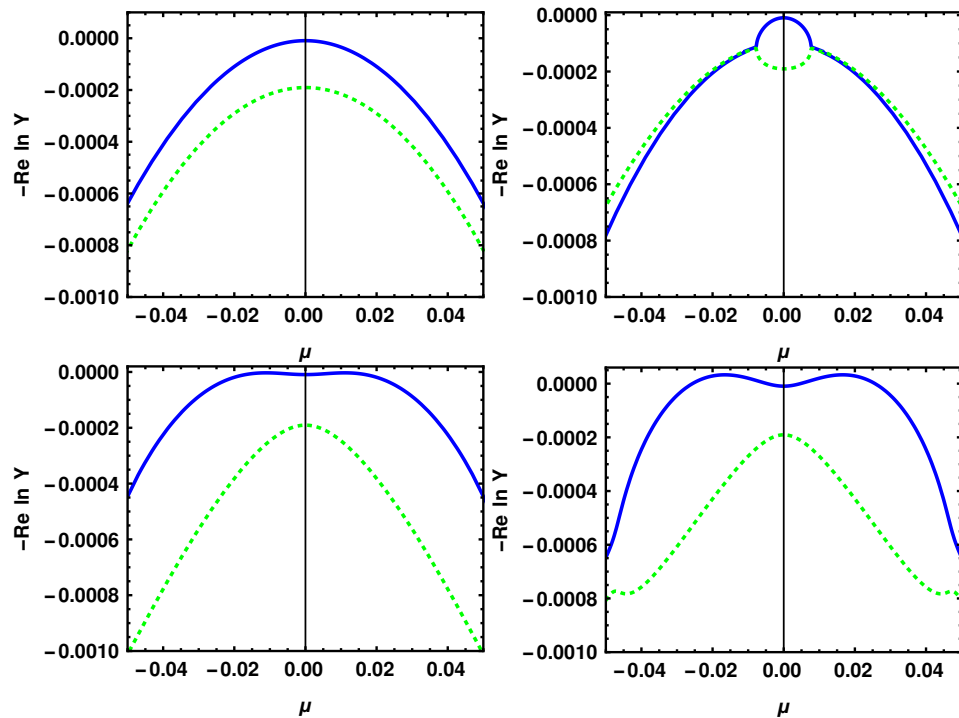


Figure 4. Curves of pseudocontinuous spectrum in the limit of large delay (21) of (12) of the CW with the largest intensity ($|A_0| \approx 0.0169$ out of another two $|A_0| \approx 0.0167$ and $|A_0| \approx 0.006$) near the LLE limit, $\eta \approx 1.707 \times 10^{-6}$, and varying $\beta = 0$ (top-left), $\beta = 1/4$ (top-right), $\beta = -1/8$ (bottom-left), $\beta = -1/4$ (bottom-right). Other parameters are as in Figure 3.

The stability condition of the CW state can be written in the form $|Y_{\pm}(i\mu)| > 1$ for all the wavenumbers μ . In particular, at zero wavenumber $\mu = 0$ we get

$$|Y_{\pm}(0)| > 1. \tag{27}$$

A CW solution satisfying this condition is stable with respect to perturbations at zero wavenumber, but may be unstable with respect to MI at nonzero wavenumbers. A possible (but not unique) way how such a MI can develop is related to the change of the sign from negative to positive of one of the two quantities $\Lambda''_{\pm}(0)$ corresponding to the greater of the two values $\Lambda''_{\pm}(0)$. Note, that both the quantities $\Lambda''_{\pm}(0)$ are always negative at $\beta = 0$ due to the inequality (11). It follows from Equation (26) that such a sign change can take place only in the case when

$$D > 0 \tag{28}$$

and, hence, $Y_{\pm}(0)$ must be real. Otherwise, B is purely imaginary and the last term in the RHS of Equation (25) vanishes. It is shown in Appendix A that in the LLE limit (14) we have $\Lambda_+(0) < \Lambda_-(0)$ and for the CW state with the highest intensity we can have $\Lambda''_-(0) > 0$ only in the anomalous dispersion regime $\beta < 0$. Out of LLE limit we can have positive $\Lambda''_{\pm}(0)$ in case of $\beta > 0$ as well (see Appendix B for numerical treatment).

Note, that the development of MI on the stable upper part of the CW branch can be correlated with the appearance of stable localized structures. In the next section we study numerically how the dispersion coefficient β affects the existence range of these structures. Remarkably, there are also scenarios out of the LLE limit where localized structures can be observed for zero and small positive β .

We note that the condition $\Lambda''(0) > 0$ precedes the appearance of MI of the CW for stronger dispersion if $Y_{\pm}(0)$ is real-valued. If it is complex-valued, MI is still possible for sufficiently strong dispersion (see Figure 5). In the LLE limit, one can derive an approximate condition for MI development (see Appendix A), and demonstrate that for typical parameters in this limit strong anomalous dispersion can lead to the instability.

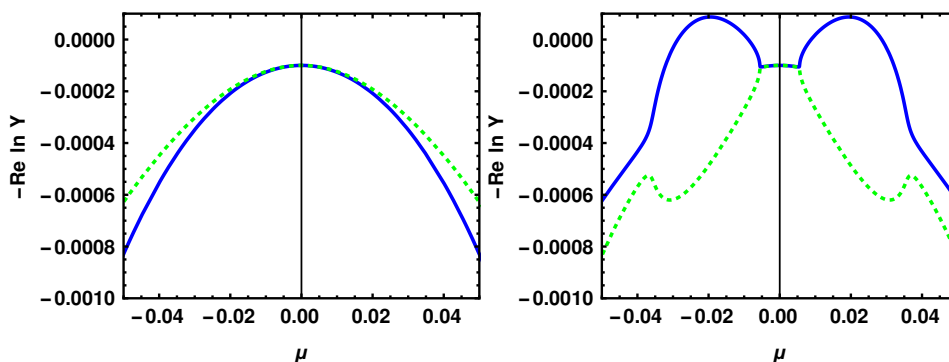


Figure 5. Curves of pseudocontinuous spectrum in the limit of large delay (21) of (12) of the CW with the largest intensity ($|A_0| \approx 0.0178$ out of another two $|A_0| \approx 0.0156$ and $|A_0| \approx 0.0065$) near the LLE limit with $\beta = 1/2$ (left) and $\beta = -1/2$ (right), and $\eta \approx 1.797 \times 10^{-6}$. Other parameters are as in Figure 3.

4. Numerical Results

In this section, we perform numerical bifurcation analysis of Equation (12) using DDE-BIFTOOL [43]. Let us start with the parameter set close to the LLE limit. We take $\sigma = \sqrt{2.5}$, $\beta = -0.5$, which corresponds to two filters (5) with $\gamma_1 = \gamma_2$, $\omega_1 = -\frac{1+\sqrt{5}}{2}\gamma_1 \approx -1.62\gamma_1$, $\omega_2 = \frac{\sqrt{5}-1}{2}\gamma_2 \approx 0.62\gamma_2$. Let $\alpha = 1$, $\omega_0 = 0$ and $\varphi = \varphi_{\epsilon}$, $\kappa = \kappa_{\epsilon}$, where

$$\kappa_{\epsilon} = \exp(-2\epsilon^2), \quad \varphi_{\epsilon} = -2\epsilon^2$$

are chosen according to analysis of DDE (13) in the limit $\epsilon \rightarrow 0$. These values directly correspond to the parameters of LLE (16) where localized structures are known to exist ($\theta = \varphi/\epsilon^2 < -\sqrt{3}$). We also pick a reference injection strength

$$\eta_\epsilon = \epsilon^3 \sqrt{\frac{8}{\sqrt{3}^3} + \frac{4}{3} \left(-\frac{\varphi_\epsilon}{\epsilon^2} - \sqrt{3}\right)}, \tag{29}$$

where three CW states are guaranteed to coexist for $\epsilon \ll 1$, and vary η near η_ϵ . The main numerical difficulty in this limit is that the delay time T and the width of the localized structures are proportional to the large quantity ϵ^{-1} . Figure 6 was obtained with $\epsilon = 0.05$, which was the smallest value of ϵ used in our simulations and corresponded to $\kappa \approx 0.995$. Similarly to the LLE [44,45] the bifurcation diagram in the left panel of this figure shows a typical S-shaped CW branch with stable lower part and modulationally unstable upper part. The branch of unstable periodic solutions bifurcates from the unstable middle part of the CW branch and it becomes stable after a fold bifurcation at $\eta \approx 0.00022$. The stable periodic solution has only a slight asymmetry in its time profile and resembles the temporal dissipative solitons of the LLE, see right panel of Figure 6.

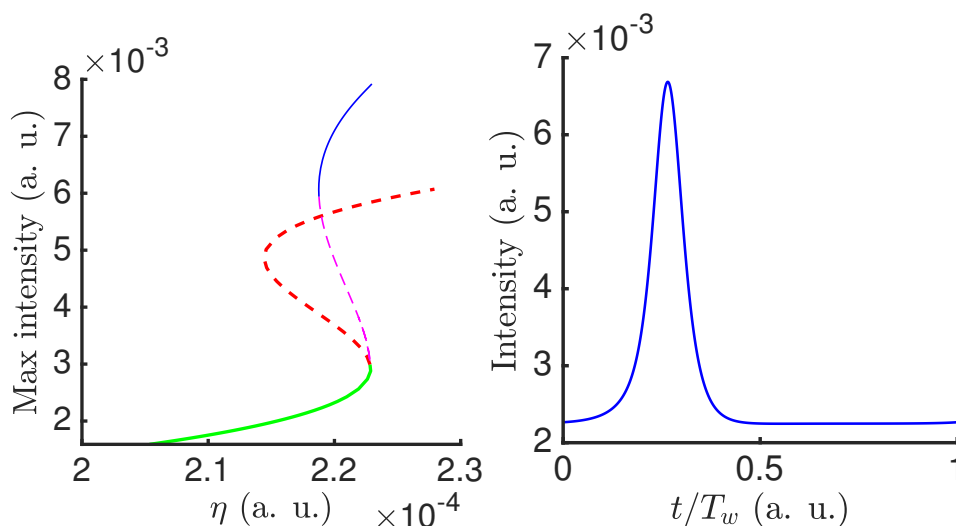


Figure 6. Left panel: One-parameter bifurcation diagram of Equation (12) with $\varphi = \varphi_\epsilon$, $\kappa = \kappa_\epsilon$, and $\epsilon = 0.05$. CW (periodic) solutions are shown by thick (thin) lines. Solid lines represent stable states and dashed lines represent unstable states. The parameter η is changed near η_ϵ defined by Equation (29). Right panel: Stable localized periodic solution for $\eta \approx 0.000223$, where $T_w \sim 1/\epsilon$ is the period of the solution controlled by the choice of delay time T . Other parameters are $\alpha = 1$, $\sigma = \sqrt{2.5}$, $\beta = -0.5$.

Thus, close to the limit $\epsilon \rightarrow 0$ the normalized second-order DDE (12) demonstrates the bifurcation structure similar to that of the LLE. Note, however, that the magnitude of the parameters σ , β and $1 - \kappa$ in the normalized Equation (12) depends on the frequency detuning of the linear filters with respect to each other in the original equivalent system (1) and (2), and stronger detuning results for fixed σ in larger $|\beta|$ as discussed in Section 2.1, and higher losses $1 - \kappa$ at the same time as discussed in Section 2.2. Therefore, it is necessary to investigate how larger values of ϵ corresponding to smaller values of the attenuation factor κ (larger losses) affect the properties of the localized solutions. For example, for the considered parameters $\sigma = \sqrt{2.5}$ and $\beta = -0.5$ from Equations (1) and (2) and the condition $\kappa_l \leq 1$ one obtains $\kappa \leq 0.4$ in (12), which is satisfied for $\epsilon \geq 0.7$.

For larger $\epsilon = 0.2$, which corresponds to $\kappa \approx 0.92$, the stable part of the periodic solution branch is split into two parts separated by two fold bifurcation points, see left panel of Figure 7. Both these parts correspond to very asymmetric localized pulses, but the second part contains wider pulses than the first one, see right panel of Figure 7.

Figures 8 and 9 show the branches of CW and periodic solutions with scaled intensity (In these figures η is shifted, more precisely, $\tilde{\eta} = \eta - \eta_\epsilon - \eta_{1,j} + 10^{-5}j$ for the left panel of Figure 8, $\tilde{\eta} = \eta - \eta_\epsilon - \eta_{2,j} + 5j\eta_{2,1}$ for the right panel, $\tilde{\eta} = \eta - \eta_\epsilon - \eta_{1,j} + 10^{-2}(j - 4)$ for the left panel of Figure 9, $\tilde{\eta} = \eta - \eta_\epsilon - \eta_{2,j} + 2 \times 10^{-3}(j - 4)$ for the right panel, and $\epsilon = \epsilon_j$, $\vec{\epsilon} = \{0.05, 0.1, 0.2, 0.3, 0.4, 0.5, 0.6, 0.7, 0.8, 0.9, 1.0\}$, $\vec{\eta}_1 = \{-1.2 \times 10^{-5}, -1.634 \times 10^{-4}, -7.69 \times 10^{-4}, -0.0039, -0.0136, -0.0245, -0.059, -0.11, -0.195, -0.347, -0.5474\}$, $\vec{\eta}_2 = \{1.413 \times 10^{-6}, 4.3 \times 10^{-6}, -1.2 \times 10^{-4}, -0.0015, -0.006, -0.019, -0.047, -0.099, -0.185 - 0.333, -0.5294\}$) obtained by increasing gradually ϵ up to 1, which corresponds to $\kappa \approx 0.135$. The width of the S-shaped area of the CW branches as well as the width of the branch of the localized solutions increases with ϵ up to $\epsilon = 0.8$ and then decreases. For $\epsilon \geq 0.4$ the upper branch of CW states stabilizes for the chosen parameter values (Figure 9, left). Asymmetric localized structures corresponding to the stable parts of the periodic solution branches with $\epsilon \geq 0.2$ in Figure 10 look similar to the those shown in the right panel of Figure 7 obtained for $\epsilon = 0.2$.

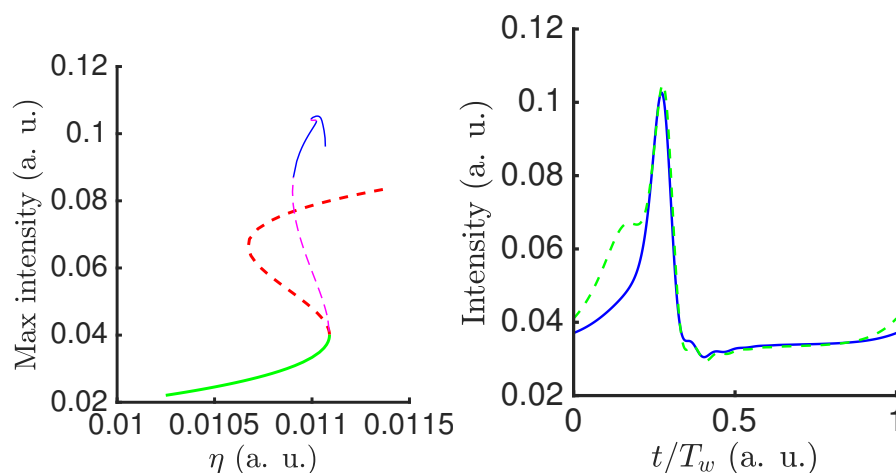


Figure 7. Left panel: One-parameter bifurcation diagram of Equation (12) with $\varphi = \varphi_\epsilon$, $\kappa = \kappa_\epsilon$, and $\epsilon = 0.2$. CW (periodic) solutions are shown by thick (thin) lines. Solid lines represent stable states and dashed lines represent unstable states. The parameter η is changed near η_ϵ defined by Equation (29). Right panel: Stable localized periodic solutions for the same η from the first (main) stable part of the periodic solution branch (solid) and the secondary stable part (dashed). Other parameters are as in Figure 6.

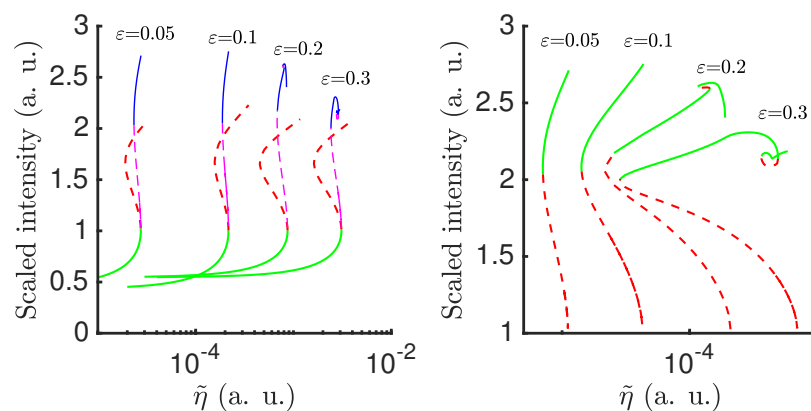


Figure 8. Bifurcation diagrams of Equation (12) obtained for different values of ϵ . Left panel: CW states cut around S-shaped bifurcation curve (thick lines) and periodic solutions (thin lines). Solid lines represent stable states and dashed lines represent unstable states, $\tilde{\eta} = \eta - \eta_\epsilon + \delta\eta(\epsilon)$ is a shifted value of η . Right panel: Branches of periodic solutions from the left panel, magnified. The intensity is scaled by ϵ^2 and other parameters are as in Figure 6.

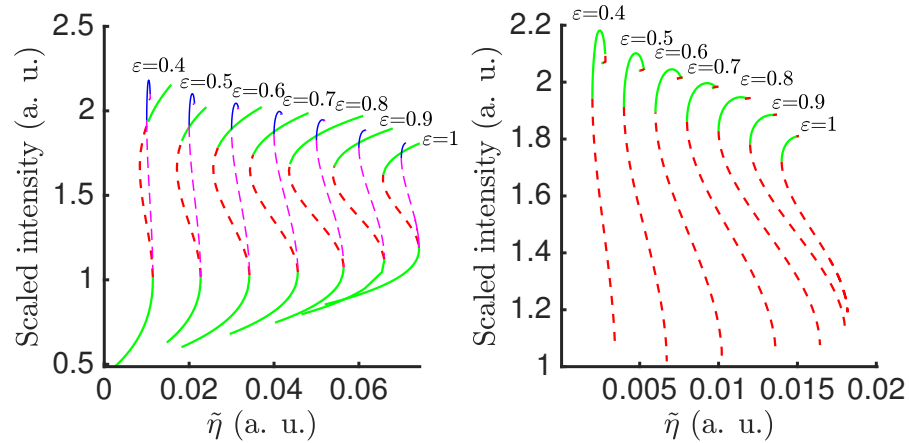


Figure 9. CW states cut around S-shaped bifurcation curve (thick lines) and periodic solutions (thin lines) of (12), where solid lines represent stable states and dashed lines represent unstable states. Right panel: Branches of periodic solutions from the left panel, magnified. The intensity is scaled by ϵ^2 , the curves from left to right correspond to $j = 5, 6, 7, 8, 9, 10, 11$, and other parameters are as in Figure 8.

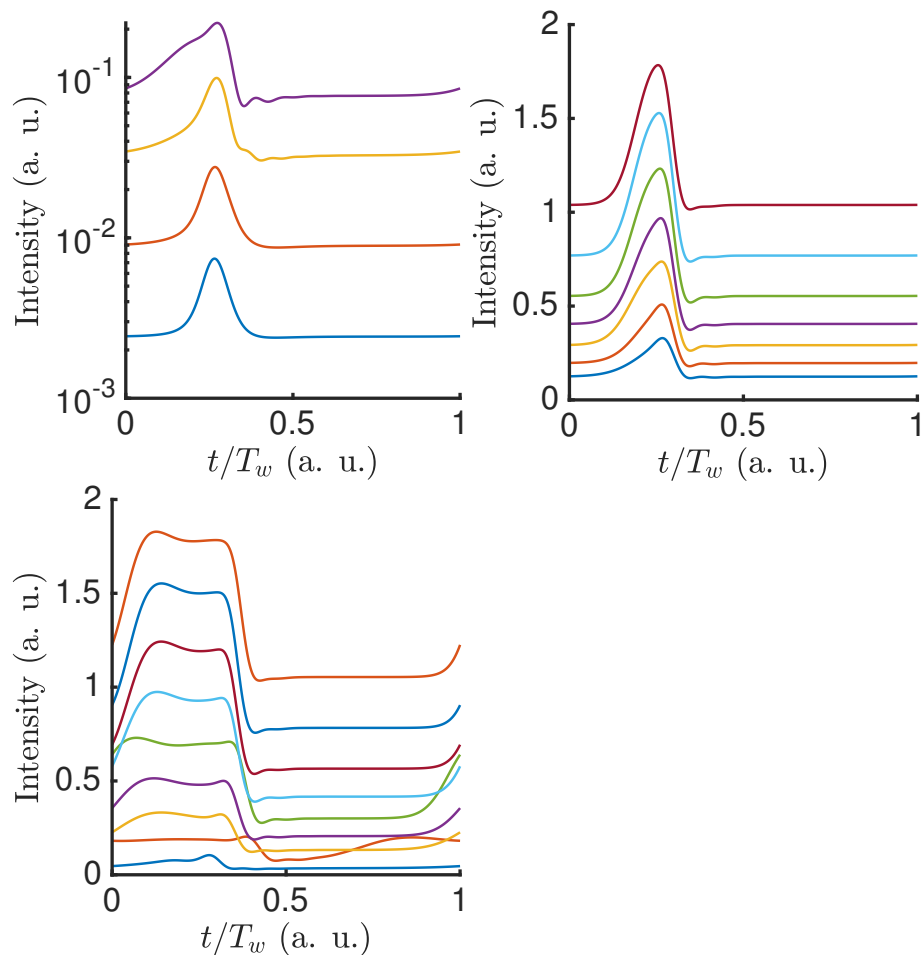


Figure 10. Top panels: Localized periodic solutions of Equation (12) from the middle points of the stable parts of the branches depicted on Figures 8 and 9 for ϵ increasing from 0.05 (bottom curve of the left upper panel) to 1 (top curve of the bottom panel). Bottom panel: Wider localized solutions from the secondary parts of the periodic solution branches for ϵ increasing from 0.2 (bottom curve) to 1 (top curve). Time is scaled by the solution period $T_w \sim \epsilon^{-1}$, which is controlled by the delay time T . Other parameters are as in Figure 8.

Finally, let us study how the variation of the effective dispersion coefficient β influences the existence range of the temporal localized structures. One can see in the top left panel of Figure 11 that near the LLE limit ($\varepsilon = 0.05$) the localized solutions can be observed only for negative $\beta < -0.05$ corresponding to the anomalous dispersion regime. It is seen that when β increases the interval of the injection rates between two fold bifurcations, where stable localized solutions exist, shrinks so that for $\beta \geq -0.06$ one can hardly see any stable localized structure in the region of S-shaped CW curve. However, by increasing ε out of the LLE limit first to $\varepsilon = 0.3$ (top right panel of Figure 11) and then to $\varepsilon = 0.5$ (bottom left panel), one can see that around $\varepsilon \approx 0.5$ localized structures can be observed for $\beta = 0$ as well. Furthermore, for $0.5 \leq \varepsilon \leq 1$ (bottom right panel) stable bright temporal dissipative solitons can be observed even with small positive β , $0 \leq \beta < 0.1$. Therefore, we conclude that out of the LLE limit temporal localized structures in the DDE model (12) could be observed not only in anomalous dispersion regime but also for positive β , although in a smaller range of the injection rates η . We have considered here only one possible way to exit the LLE limit in a continuous manner, however our preliminary numerical simulations suggest that there are many possible combinations of values of κ , η , φ , and β away from the LLE limit, where stable or unstable temporally localized structures can be observed. We leave this question to further studies, and, in particular, for experimentally justified parameters.

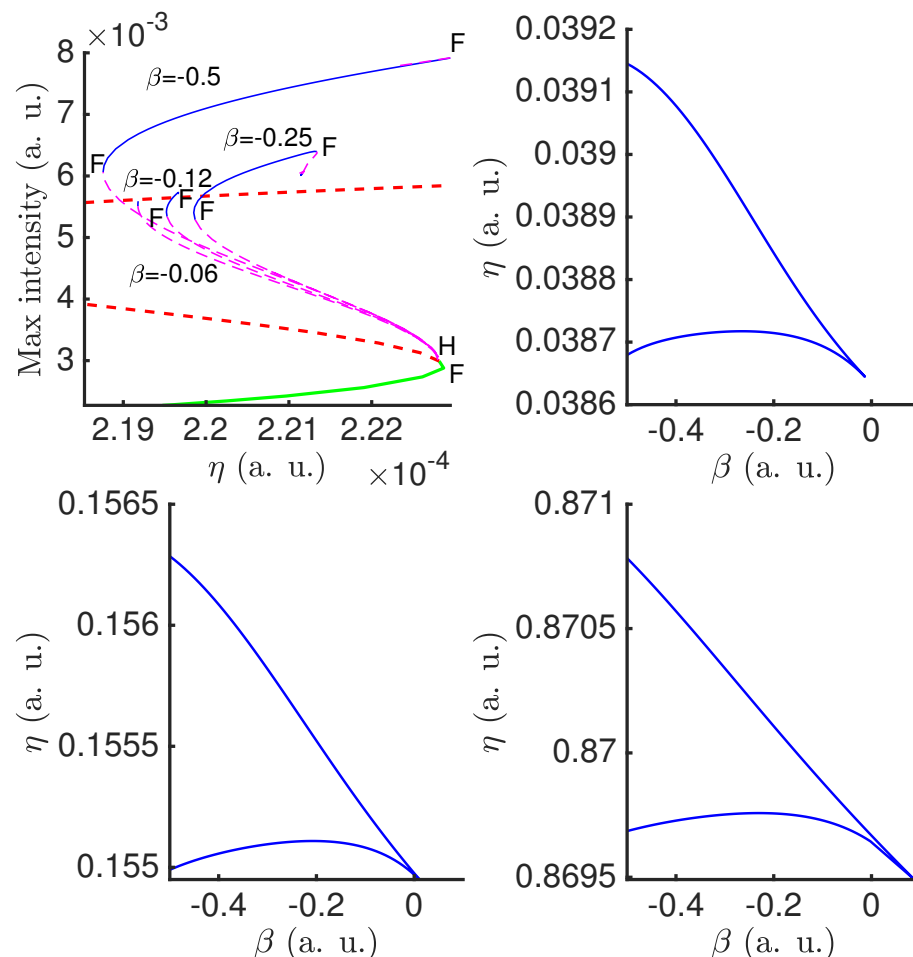


Figure 11. Top left: Bifurcation diagram of Equation (12) for $\varepsilon = 0.05$ and various values of β . Thick lines indicate CW solutions cut around S-shaped bifurcation curve, while thin lines correspond to periodic solutions. Solid (dashed) lines represent stable (unstable) solutions. Fold bifurcations are marked by F and Hopf bifurcations are marked by H. Other panels show fold bifurcations of the localized periodic solutions of (12) on the plane of two parameters, β and η . They correspond to $\varepsilon = 0.3$ (top right), $\varepsilon = 0.5$ (bottom left), and $\varepsilon = 1.0$ (bottom right). Other parameters are as in Figure 8.

In this section we have demonstrated the existence of bright localized structures of the second order DDE model (12). It follows from this result that such kind of structures should also exist in the original set of two DDEs (1) and (2). We can use this theory then to find parameters for (1) and (2) where localized structures exist (see Figure 12).

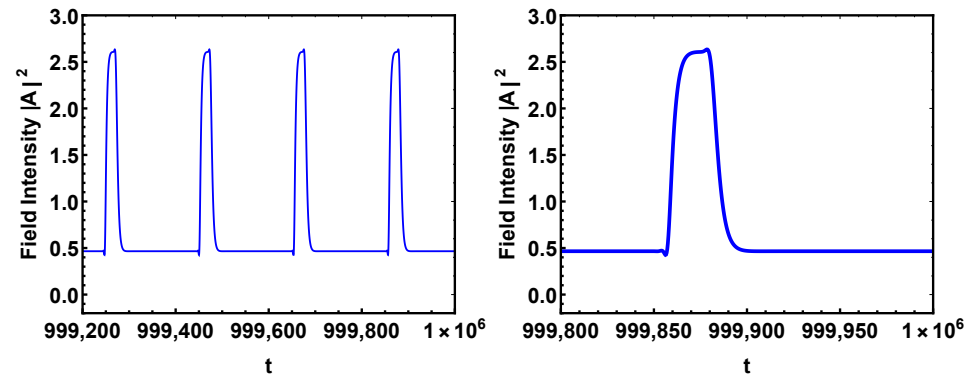


Figure 12. Periodic pulse train solution $A(t)$ of (1) and (2) (**left**) and single pulse (**right**), where the parameters are $\gamma_1 = 1$, $\omega_1 \approx 1.29$, $\gamma_2 \approx 0.26$, $\omega_2 \approx -0.034$, $\kappa_1 \approx 0.68$, $\phi \approx -4.17$, $\eta_0 \approx 1.65$, $\alpha = 1.5$, $T = 200$. In the normalized Equation (12) these values correspond to $\sigma = 3.23$, $\beta = 1$, $\kappa = 0.25$, $\varphi \approx -3.383$, $\eta = 1$.

5. Conclusions

We have considered a DDE model of an optically injected ring Kerr cavity with two spectral filters having different widths and central frequencies. We have derived a normalized complex-valued second order DDE (12), which is similar to real-valued DDE reported in [39]. This equation can be considered as a generalization of the Ikeda map, which explicitly contains second-order dispersion coefficient at zero frequency as a parameter. We have derived an admissibility relation for these parameters, analyzed stability of the CW solutions of this model in the limit of large delay, and demonstrated the effect of strong dispersion on the development of modulational instability. We have shown that in the limit of small losses and weak injection the DDE model can be reduced to a generalized version of the well known LLE, which is known to have dissipative soliton solutions. We have performed numerical bifurcation analysis of CW solutions and temporal localized structures using DDE-BIFTOOL package [43] and demonstrated qualitative similarity of the solutions of the DDE model with those of the LLE in the regime of anomalous dispersion ($\beta < 0$) in the corresponding limit. Moreover, out of LLE limit one can observe numerically stable asymmetric bright localized structures not only in the anomalous dispersion regime, but also at zero and small positive values of β , albeit in a shrinkingly smaller interval of existence. This is in agreement with the results of Ref. [46] obtained using an extended LLE with the third order dispersion term included. Experimental observations of asymmetric temporal Kerr cavity solitons near zero dispersion point, where higher order dispersion comes into play, were reported in [47].

To summarize, we have proposed theoretically a Kerr cavity scheme, where the dispersion introduced by two spectral filters with different central frequencies can lead to the development of modulational instability and appearance of stable temporal cavity solitons even when the material dispersion is negligible. This scheme is different from the traditional Kerr cavity setups for frequency comb generation, where chromatic dispersion of the intracavity material plays a crucial role in soliton formation. The modeling approach we have developed is also suitable for the analysis of more complex systems with two spectral filters, such as Mamyshev oscillators. Investigation of short pulse generation in Mamyshev oscillators using the theoretical basis developed here might be a subject for future research.

Author Contributions: Conceptualization, A.G.V. and A.P.; methodology, A.G.V.; software, A.P.; validation, A.P. and A.G.V.; formal analysis, A.P.; investigation, A.P.; writing—original draft preparation, A.P.; writing—review and editing, A.G.V.; visualization, A.P.; supervision, A.G.V.; project administration, A.G.V.; funding acquisition, A.G.V. All authors have read and agreed to the published version of the manuscript.

Funding: The authors acknowledge the support of the DFG Project 445430311.

Institutional Review Board Statement: Not applicable.

Informed Consent Statement: Not applicable.

Data Availability Statement: Not applicable.

Acknowledgments: Not applicable.

Conflicts of Interest: The authors have no conflicts of interest to declare.

Appendix A. MI in the LLE Limit

Linear stability of the CW solutions of the classical Lugiato-Lefever equations was studied analytically and numerically in a number of works, see e.g., Refs. [48–50] for both the normal and anomalous dispersion regimes. In this Appendix we consider the DDE model (12) in the LLE limit, where this model can be reduced to the generalized LLE (16) with the additional diffusion (spectral filtering) term $(\sigma^2 - 2)/2$, which exerts a stabilizing effect on the CW solutions. A detailed linear stability analysis of the generalized LLE model (12) is beyond the scope of this paper. We present here only some analytical results concerning the sign change of one of the two quantities $\Lambda_{\pm}''(0)$ (see Equation (25)), which can be a precursor of the MI.

Without the loss of generality we can assume that $\alpha = 1$ and $k = 1$. Substituting (14) and $A_0 = \epsilon u_0 + \mathcal{O}(\epsilon^2)$ into (23)–(25) and using $\Lambda_{\pm}(0) = -\Re \ln Y_{\pm}(0)$ we obtain:

$$\Lambda_{\pm}(0) = \epsilon^2 \left(1 \mp \Re \sqrt{\tilde{D}} \right) + \mathcal{O}(\epsilon^3), \quad \tilde{D} = -\left(\theta + 3u_0^2 \right) \left(\theta + u_0^2 \right), \quad (A1)$$

$$\Lambda_{\pm}''(0) = 2 - \sigma \pm \Re \left[\frac{2\beta(2u_0^2 + \theta)}{\sqrt{\tilde{D}}} \right] + \mathcal{O}(\epsilon). \quad (A2)$$

where $\Lambda_{\pm}''(0)$ can be positive only when $\tilde{D} > 0$, i.e., for $-\frac{\theta}{3} < u_0^2 < -\theta$. We see from (A1) and (A2) that for $\tilde{D} > 0$ in the LLE limit we have $\Lambda_+(0) < \Lambda_-(0)$ and the curvature $\Lambda_{\pm}''(0)$ can be positive only for

$$\beta(2u_0^2 + \theta) < 0. \quad (A3)$$

Let us consider the case when Equation (20) has three real roots, which similarly to the standard LLE takes place for $\theta < -\sqrt{3}$. Taking a real root $u_0^2 = a^2$ of Equation (20) we can express the remaining two roots as

$$u_{0\pm}^2 = \frac{1}{2} \left(\pm \sqrt{-4a^2\theta - 3a^4 - 4 - a^2 - 2\theta} \right), \quad (A4)$$

where three distinct roots are real for $\theta < -\sqrt{3}$ and

$$-\frac{2\theta}{3} - \frac{2}{3}\sqrt{\theta^2 - 3} < a^2 < -\frac{2\theta}{3} + \frac{2}{3}\sqrt{\theta^2 - 3}. \quad (A5)$$

From this condition it follows that $2a^2 + \theta > 0$ for all $-\frac{4}{\sqrt{5}} < \theta < -\sqrt{3}$. Furthermore, the condition that $u_{0\pm}^2 < a^2$ for both the roots defined by (A4) is also possible only for $2a^2 + \theta > 0$. Therefore it follows from (A3) that for any $\theta < -\sqrt{3}$ the CW state with the highest intensity can have $\Lambda_{\pm}''(0) > 0$ only in the anomalous dispersion regime $\beta < 0$.

Since the condition $\Lambda''(0) > 0$ is not sufficient for the development of MI of a CW state, we assume further in (21) with $k = \alpha = 1$ that $\Im\lambda = \varepsilon w$. Then up to order ε^2 we obtain:

$$\Lambda_{\pm}(w) \approx - \left[2 + \frac{w^2(\sigma^2 - 2)}{2} \pm \sqrt{D(w)} \right] \varepsilon^2,$$

where $D(w) = -(u_0^2 + \beta w^2 - \theta)(3u_0^2 + \beta w^2 - \theta)$. We can find the frequencies w at which the MI can be observed using the conditions

$$\Lambda'(w) = 0, \quad \Lambda_-(w) = 0. \tag{A6}$$

In particular, in the normal dispersion regime ($\beta > 0$) solving (A6) with respect to w^2 and θ we obtain

$$w^2 \approx \frac{4}{\sigma^2 - 2} \left[\frac{u_0^2 \beta}{\sqrt{4\beta^2 + (\sigma^2 - 2)^2}} - 1 \right] > 0 \tag{A7}$$

and two solutions for θ

$$-\theta \approx \frac{u_0^2 \left[2(\sigma^2 - 2) + \sqrt{4\beta^2 + (\sigma^2 - 2)^2} \right] - 4\beta}{\sigma^2 - 2} > 4, \tag{A8}$$

$$-\theta \approx \frac{1}{\sigma^2 - 2} \left\{ u_0^2 \left[2(\sigma^2 - 2) + \frac{4\beta^2 - (\sigma^2 - 2)^2}{\sqrt{4\beta^2 + (\sigma^2 - 2)^2}} \right] - 4\beta \right\} > 2\sqrt{3}. \tag{A9}$$

Since according to (A7)–(A9) both w^2 and $-\theta$ increase with u_0 , the value of $-\theta$ corresponding to $w = 0$ gives the lower bound of the detuning parameter, for which the development of MI is possible. We note that for $w = 0$ and $\theta < 0$ we have $D(0) < 0$, and $\Lambda_-(0) \neq 0$, hence MI is not possible, and the lower bound obtained using $w = 0$ is not tight and provides a necessary condition for the MI. It follows from Equation (A7) that for $w = 0$ we get $u_0^2 = \frac{\sqrt{4\beta^2 + (\sigma^2 - 2)^2}}{\beta} > 2$. Substituting this expression into (A8) and (A9) yields the following expression for the lower bound of the MI:

$$-\theta \approx \frac{2\sqrt{4\beta^2 + (\sigma^2 - 2)^2} \pm (\sigma^2 - 2)}{\beta}, \tag{A10}$$

where the sign "+" ("−") corresponds to Equation (A8) [Equation (A9)]. The expression in the right hand side of Equation (A10) achieves its minimal value $-\theta \approx 2\sqrt{3}$ at $\sigma^2 = 2 \mp \frac{2\beta}{\sqrt{3}}$. Therefore, for $-\theta < 2\sqrt{3}$ MI is not possible in the normal dispersion regime.

From the previous paragraph we see that in normal dispersion regime the MI is possible only for sufficiently large $-\theta > 2\sqrt{3}$. In the anomalous dispersion case ($\beta < 0$) by solving Equation (A6) we get the following expression for the MI frequencies

$$w^2 \approx - \frac{4}{\sigma^2 - 2} \left[\frac{u_0^2 \beta}{\sqrt{4\beta^2 + (\sigma^2 - 2)^2}} + 1 \right] > 0$$

with $u_0 > \frac{\sqrt{4\beta^2 + (\sigma^2 - 2)^2}}{-\beta} > 2$ and two solutions for the detuning parameter θ :

$$-\theta \approx \frac{u_0^2 \left[2(\sigma^2 - 2) - \sqrt{4\beta^2 + (\sigma^2 - 2)^2} \right] - 4\beta}{\sigma^2 - 2},$$

and

$$-\theta \approx \frac{1}{\sigma^2 - 2} \left\{ u_0^2 \left[2(\sigma^2 - 2) + \frac{-4\beta^2 + (\sigma^2 - 2)^2}{\sqrt{4\beta^2 + (\sigma^2 - 2)^2}} \right] - 4\beta \right\}.$$

Here, the coefficients by u_0^2 can change sign depending on the parameters, hence there is no clear lower boundary for $-\theta$ in contrast to normal dispersion regime. Moreover, we could numerically observe MI for $\sigma = \sqrt{2.5}$, see Figures 4 and 5. Finally, we conclude that while it is possible to observe MI in the case of anomalous dispersion, in normal dispersion case that can be done only for sufficiently large $-\theta > 2\sqrt{3}$.

Appendix B. Examples of MI Out of LLE Limit

Finally, we consider some examples of specific CWs, where relation (26) can be simplified, so that conditions for the change of curvature of $\Lambda_{\pm}(\xi)$ at $\xi = 0$ can be obtained explicitly, and then MI can be demonstrated numerically for close parameters.

For that, let us first study the conditions (27) and (28), which ensure that the CW is stable for $\beta = 0$ and that $\Lambda''(0)$ can become positive for some $\beta \neq 0$, and introduce auxiliary variable

$$\zeta = \cos(\alpha A_0^2 + \varphi),$$

in Equations (17) and (18). Then we get $\sin(\alpha A_0^2 + \varphi) = \pm \sqrt{1 - \zeta^2}$ and Equation (19) can be rewritten in the form $A_0 = \frac{\eta}{\sqrt{\kappa + 1 - 2\sqrt{\kappa}\zeta}}$ with $-1 \leq \zeta \leq 1$.

For $\sin[2(\alpha A_0^2 + \varphi)] < 0$ using the relations (23) and (24) the inequalities (27) and (28) can be rewritten in the form

$$\frac{1 - |\zeta|}{\sqrt{1 - \zeta^2}} < \alpha A_0^2 \leq \frac{1}{\sqrt{1 - \zeta^2}} \left(|\zeta| + \frac{1 + \kappa}{2\sqrt{\kappa}} \right). \tag{A11}$$

Furthermore, from (26) one can see that for $\alpha A_0^2 > \frac{\sqrt{1 - \zeta^2}}{|\zeta|} > \frac{1 - |\zeta|}{\sqrt{1 - \zeta^2}}$ we have $\mathcal{B} > 0$ when $\Lambda_+(0) < \Lambda_-(0) < 0$, and $\mathcal{B} < 0$ when $\Lambda_-(0) < \Lambda_+(0) < 0$. Hence it follows from (25) that the sign change of one of the two quantities $\Lambda'_{\pm}(0)$ corresponding to larger $\Lambda_{\pm}(0)$, which can lead to a MI of the CW solution, can occur only for $\beta < 0$. In the LLE limit one can see that this scenario usually corresponds to the change of the curvature sign of $\Lambda(\mu)$ of the upper part of the CW branch (see Figure 3) in anomalous dispersion regime.

Alternatively, for $\frac{1 - |\zeta|}{\sqrt{1 - \zeta^2}} < \alpha A_0^2 < \frac{\sqrt{1 - \zeta^2}}{|\zeta|}$ we have $\mathcal{B} < 0$ when $\Lambda_+(0) < \Lambda_-(0) < 0$, and $\mathcal{B} > 0$ when $\Lambda_-(0) < \Lambda_+(0) < 0$. Hence, in this case the sign change of the curvature can occur for $\beta > 0$.

For $\sin[2(\alpha A_0^2 + \varphi)] > 0$ instead of (A11) we get the inequalities

$$|\zeta| + 1 < \alpha A_0^2 \sqrt{1 - \zeta^2} \leq |\zeta| + \frac{1 + \kappa}{2\sqrt{\kappa}}, \tag{A12}$$

which imply that $A_0 > \frac{1}{\sqrt{\alpha}}$, which is incompatible with the LLE limit, where A_0 is asymptotically small. Since $|\zeta| \leq 1$, from (24) one can see that for $A_0 = 0$ we have $D \leq 0$. In particular, according to Equations (23) and (24) together with the inequality $\sin[2(\alpha A_0^2 + \varphi)] > 0$, for $D = 0$ we get $Y_{\pm}(0) = -\frac{1}{\sqrt{\kappa}}$ for $\sin(\alpha A_0^2 + \varphi) > 0$ and $Y_{\pm}(0) = \frac{1}{\sqrt{\kappa}}$ for $\sin(\alpha A_0^2 + \varphi) < 0$. Therefore, for larger A_0 and D we have $\Lambda_-(0) < \Lambda_+(0) < 0$ for $\mathcal{B} > 0$ and $\Lambda_+(0) < \Lambda_-(0) < 0$ for $\mathcal{B} < 0$. Hence, it follows from (25) that in this case the change of curvature can be observed for $\beta > 0$.

Let us consider a simple case where $\varphi = -\alpha A_0^2 + \pi/2$ in Equation (12) and, therefore, $\cos(\alpha A_0^2 + \varphi) = 0$ in Equation (19). Hence, we get $A_0 = \frac{\eta}{\sqrt{1 + \kappa}} < \eta$, which corresponds to the CW with the lowest intensity in case of bistable S-shaped CW branch. Furthermore,

from (23) we obtain $D = \frac{\alpha^2 \eta^4}{(\kappa+1)^2} - 1$ and $Y_+(0) = \frac{1}{\sqrt{\kappa}} \left(\frac{\alpha \eta^2}{\kappa+1} + \sqrt{D} \right)$. Therefore, from (25) and (A12) with sufficiently large β we can have

$$\Lambda_+''(0) = 2 - \sigma^2 + \frac{2\beta}{\sqrt{\frac{\alpha^2 \eta^4}{(\kappa+1)^2} - 1}} > 0, \quad 1 + \kappa < \alpha \eta^2 < \frac{(1 + \kappa)^2}{2\sqrt{\kappa}}.$$

This condition is reminiscent of the MI condition of a CW in the anomalous dispersion regime in the case of CW solutions of a semiconductor laser model [31], though second-order dispersion coefficient β is multiplied here not by α but by a function of α, η, κ . Similarly to the case of a laser under optical injection [32], this condition manifests the change of curvature of $\Lambda(\xi)$ at $\xi = 0$ for some $\beta > 0$, and it precedes appearance of a MI for larger β , which can be observed numerically (see Figure A1, top).

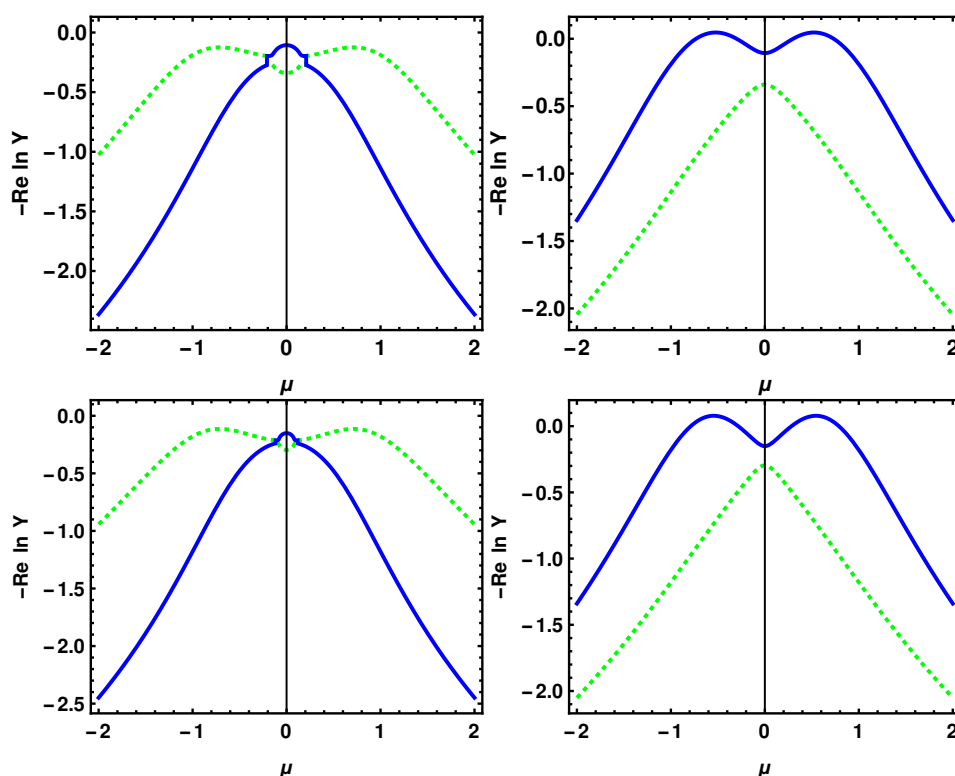


Figure A1. Curves of pseudocontinuous spectrum in the limit of large delay (21) of (12) of the CW with the lowest intensity $A_0 = \frac{\eta}{\sqrt{1+\kappa}}$ for $\zeta = \frac{\pi}{2}, \eta = 1.285$ (top) and the largest intensity (A13) for $\zeta = \pi/6, \eta = 0.975$ with $\beta = -0.3$ (top-left), $\beta = 0.3$ (top-right), $\beta = -0.1$ (bottom-left) and $\beta = 0.1$ (bottom-right). Other parameters are $\kappa = 0.8, \sigma = \sqrt{2.5}, \alpha = 1$.

The most usual way to find a localized structure in form of a bright dissipative soliton, is to look for three coexisting CWs, where CW with the largest field intensity A_0^2 is modulationally unstable. Indeed, for $\varphi = -\alpha A_0^2 + \frac{\pi}{6}$, where $\zeta = \frac{\sqrt{3}}{2}$, the CW takes the form

$$A_0 = \frac{\eta}{2 - \sqrt{3}\kappa} \sqrt{3 + \frac{1 - \sqrt{3}\kappa}{\kappa^2 - \sqrt{3}\kappa + 1}} > \eta. \tag{A13}$$

and the condition $\Lambda''(0) \geq 0$ takes the form

$$2 - \sigma^2 + \frac{2\beta(\sqrt{3}\alpha A_0^2 + 1)}{\sqrt{\alpha^2 A_0^4 - 2\sqrt{3}\alpha A_0^2 - 1}} \geq 0, \quad 2 + \sqrt{3} < \alpha A_0^2 \leq \frac{\kappa + \sqrt{3}\sqrt{\kappa} + 1}{\sqrt{\kappa}}.$$

Similarly, the change of curvature of $\Lambda(\xi)$ at $\xi = 0$ can occur only for $\beta > 0$, where also a MI can be observed (see Figure A1, bottom). We can use the CW (A13) by choosing corresponding parameter φ to find parameters where localized structures exist, and obtain parameters for the original system (1) and (2) to obtain these structures in numerical simulations (see Figure 12).

References

1. Fortier, T.; Baumann, E. 20 years of developments in optical frequency comb technology and applications. *Commun. Phys.* **2019**, *2*, 153. [[CrossRef](#)]
2. Kippenberg, T.J.; Gaeta, A.L.; Lipson, M.; Gorodetsky, M.L. Dissipative Kerr solitons in optical microresonators. *Science* **2018**, *361*, eaan8083. [[CrossRef](#)]
3. Bao, H.; Cooper, A.; Rowley, M.; Di Lauro, L.; Totero Gongora, J.S.; Chu, S.T.; Little, B.E.; Oppo, G.L.; Morandotti, R.; Moss, D.J.; et al. Laser cavity-soliton microcombs. *Nat. Photonics* **2019**, *13*, 384–389. [[CrossRef](#)]
4. Wang, W.; Wang, L.; Zhang, W. Advances in soliton microcomb generation. *Adv. Photonics* **2020**, *2*, 034001. [[CrossRef](#)]
5. Weiner, A.M. Cavity solitons come of age. *Nat. Photonics* **2017**, *11*, 533–535. [[CrossRef](#)]
6. Herr, T.; Brasch, V.; Jost, J.D.; Wang, C.Y.; Kondratiev, N.M.; Gorodetsky, M.L.; Kippenberg, T.J. Temporal solitons in optical microresonators. *Nat. Photonics* **2014**, *8*, 145–152. [[CrossRef](#)]
7. Boutabba, N.; Eleuch, H. Slowing light control for a soliton-pair. *Appl. Math. Inf. Sci.* **2013**, *7*, 1505. [[CrossRef](#)]
8. Englebert, N.; De Lucia, F.; Parra-Rivas, P.; Arabí, C.M.; Sazio, P.J.; Gorza, S.P.; Leo, F. Parametrically driven Kerr cavity solitons. *Nat. Photonics* **2021**, *15*, 857–861. [[CrossRef](#)]
9. Leo, F.; Coen, S.; Kockaert, P.; Gorza, S.P.; Emplit, P.; Haelterman, M. Temporal cavity solitons in one-dimensional Kerr media as bits in an all-optical buffer. *Nat. Photonics* **2010**, *4*, 471–476. [[CrossRef](#)]
10. Williams, K.; Thompson, M.; White, I. Long-wavelength monolithic mode-locked diode lasers. *New J. Phys.* **2004**, *6*, 179. [[CrossRef](#)]
11. Turaev, D.; Vladimirov, A.G.; Zelik, S. Long-Range Interaction and Synchronization of Oscillating Dissipative Solitons. *Phys. Rev. Lett.* **2012**, *108*, 263906. [[CrossRef](#)] [[PubMed](#)]
12. Vladimirov, A.G.; Gurevich, S.V.; Tlidi, M. Effect of Cherenkov radiation on localized-state interaction. *Phys. Rev. A* **2018**, *97*, 013816. [[CrossRef](#)]
13. Vladimirov, A.G.; Tlidi, M.; Taki, M. Dissipative soliton interaction in Kerr resonators with high-order dispersion. *Phys. Rev. A* **2021**, *103*, 063505. [[CrossRef](#)]
14. Dong, X.; Spiess, C.; Bucklew, V.G.; Renninger, W.H. Chirped-pulsed Kerr solitons in the Lugiato-Lefever equation with spectral filtering. *Phys. Rev. Res.* **2021**, *3*, 033252. [[CrossRef](#)]
15. Mamyshev, P. All-optical data regeneration based on self-phase modulation effect. In Proceedings of the 24th European Conference on Optical Communication, ECOC'98 (IEEE Cat. No. 98TH8398), Madrid, Spain, 20–24 September 1998; Volume 1, pp. 475–476.
16. Liu, Z.; Ziegler, Z.M.; Wright, L.G.; Wise, F.W. Megawatt peak power from a Mamyshev oscillator. *Optica* **2017**, *4*, 649–654. [[CrossRef](#)] [[PubMed](#)]
17. Ikeda, K. Multiple-valued stationary state and its instability of the transmitted light by a ring cavity system. *Opt. Commun.* **1979**, *30*, 257–261. [[CrossRef](#)]
18. Lang, R.; Kobayashi, K. External optical feedback effects on semiconductor injection laser properties. *IEEE J. Quantum Electron.* **1980**, *16*, 347–355. [[CrossRef](#)]
19. Vladimirov, A.G.; Turaev, D. New model for mode-locking in semiconductor lasers. *Radiophys. Quant. Electron.* **2004**, *47*, 857–865. [[CrossRef](#)]
20. Vladimirov, A.G.; Turaev, D. Model for passive mode-locking in semiconductor lasers. *Phys. Rev. A* **2005**, *72*, 033808. [[CrossRef](#)]
21. Vladimirov, A.G.; Turaev, D.; Kozyreff, G. Delay differential equations for mode-locked semiconductor lasers. *Opt. Lett.* **2004**, *29*, 1221–1223. [[CrossRef](#)]
22. Viktorov, E.A.; Mandel, P.; Vladimirov, A.G.; Bandelow, U. Model for mode locking in quantum dot lasers. *Appl. Phys. Lett.* **2006**, *88*, 201102. [[CrossRef](#)]
23. Viktorov, E.A.; Mandel, P.; Huyet, G. Long-cavity quantum dot laser. *Opt. Lett.* **2007**, *32*, 1268–1270. [[CrossRef](#)] [[PubMed](#)]
24. Rossetti, M.; Bardella, P.; Montrosset, I. Modeling passive mode-locking in quantum dot lasers: A comparison between a finite-difference traveling-wave model and a delayed differential equation approach. *IEEE J. Quantum Electron.* **2011**, *47*, 569–576. [[CrossRef](#)]
25. Vladimirov, A.G.; Kovalev, A.V.; Viktorov, E.A.; Rebrova, N.; Huyet, G. Dynamics of a class-a nonlinear mirror mode-locked laser. *Phys. Rev. E* **2019**, *100*, 012216. [[CrossRef](#)] [[PubMed](#)]
26. Vladimirov, A.G.; Suchkov, S.; Huyet, G.; Turitsyn, S.K. Delay-differential-equation model for mode-locked lasers based on nonlinear optical and amplifying loop mirrors. *Phys. Rev. A* **2021**, *104*, 033525. [[CrossRef](#)]
27. Vladimirov, A.G.; Panajotov, K.; Tlidi, M. Orthogonally polarized frequency combs in a mode-locked VECSEL. *Opt. Lett.* **2020**, *45*, 252–255. [[CrossRef](#)]

28. Slepneva, S.; Kelleher, B.; O'Shaughnessy, B.; Hegarty, S.; Vladimirov, A.; Huyet, G. Dynamics of Fourier domain mode-locked lasers. *Opt. Express* **2013**, *21*, 19240–19251. [[CrossRef](#)]
29. Slepneva, S.; O'Shaughnessy, B.; Kelleher, B.; Hegarty, S.; Vladimirov, A.; Lyu, H.C.; Karnowski, K.; Wojtkowski, M.; Huyet, G. Dynamics of a short cavity swept source OCT laser. *Opt. Express* **2014**, *22*, 18177–18185. [[CrossRef](#)] [[PubMed](#)]
30. Heuck, M.; Blaaberg, S.; Mørk, J. Theory of passively mode-locked photonic crystal semiconductor lasers. *Opt. Express* **2010**, *18*, 18003–18014. [[CrossRef](#)]
31. Pimenov, A.; Slepneva, S.; Huyet, G.; Vladimirov, A.G. Dispersive Time-Delay Dynamical Systems. *Phys. Rev. Lett.* **2017**, *118*, 193901. [[CrossRef](#)]
32. Pimenov, A.; Amiranashvili, S.; Vladimirov, A.G. Temporal cavity solitons in a delayed model of a dispersive cavity ring laser. *Math. Model. Nat. Phenom.* **2020**, *15*, 47. [[CrossRef](#)]
33. Schelte, C.; Camelin, P.; Marconi, M.; Garnache, A.; Huyet, G.; Beaudoin, G.; Sagnes, I.; Giudici, M.; Javaloyes, J.; Gurevich, S. Third order dispersion in time-delayed systems. *Phys. Rev. Lett.* **2019**, *123*, 043902. [[CrossRef](#)] [[PubMed](#)]
34. Grelu, P.; Akhmediev, N. Dissipative solitons for mode-locked lasers. *Nat. Photonics* **2012**, *6*, 84–92. [[CrossRef](#)]
35. Lugiato, L.A.; Lefever, R. Spatial dissipative structures in passive optical systems. *Phys. Rev. Lett.* **1987**, *58*, 2209. [[CrossRef](#)]
36. Maleki, L.; Ilchenko, V.; Savchenkov, A.; Liang, W.; Seidel, D.; Matsko, A. High performance, miniature hyper-parametric microwave photonic oscillator. In Proceedings of the 2010 IEEE International Frequency Control Symposium, Newport Beach, CA, USA, 2–4 June 2010; pp. 558–563.
37. Matsko, A.B.; Savchenkov, A.A.; Liang, W.; Ilchenko, V.S.; Seidel, D.; Maleki, L. Mode-locked Kerr frequency combs. *Opt. Lett.* **2011**, *36*, 2845–2847. [[CrossRef](#)]
38. Chembo, Y.K.; Menyuk, C.R. Spatiotemporal Lugiato-Lefever formalism for Kerr-comb generation in whispering-gallery-mode resonators. *Phys. Rev. A* **2013**, *87*, 053852. [[CrossRef](#)]
39. Kashchenko, I.S. Local dynamics of equations with large delay. *Comput. Math. Math. Phys.* **2008**, *48*, 2172–2181. [[CrossRef](#)]
40. Kolokolnikov, T.; Nizette, M.; Erneux, T.; Joly, N.; Bielawski, S. The Q-switching instability in passively mode-locked lasers. *Phys. D Nonlinear Phenom.* **2006**, *219*, 13–21. [[CrossRef](#)]
41. Wolfrum, M.; Yanchuk, S. Eckhaus instability in systems with large delay. *Phys. Rev. Lett.* **2006**, *96*, 220201. [[CrossRef](#)]
42. Yanchuk, S.; Wolfrum, M. A Multiple Time Scale Approach to the Stability of External Cavity Modes in the Lang-Kobayashi System Using the Limit of Large Delay. *SIAM J. Appl. Dyn. Syst.* **2010**, *9*, 519–535. [[CrossRef](#)]
43. Engelborghs, K.; Luzyanina, T.; Samaey, G. DDE-BIFTOOL v.2.00: A MATLAB package for bifurcation analysis of delay differential equations. In *Technical Report TW-330*; Department of Computer Science, K.U.Leuven: Leuven, Belgium, 2001.
44. Scroggie, A.; Firth, W.; McDonald, G.; Tlidi, M.; Lefever, R.; Lugiato, L.A. Pattern formation in a passive Kerr cavity. *Chaos Solitons Fractals* **1994**, *4*, 1323–1354. [[CrossRef](#)]
45. Leo, F.; Gelens, L.; Emplit, P.; Haelterman, M.; Coen, S. Dynamics of one-dimensional Kerr cavity solitons. *Opt. Express* **2013**, *21*, 9180–9191. [[CrossRef](#)] [[PubMed](#)]
46. Parra-Rivas, P.; Gomila, D.; Gelens, L. Coexistence of stable dark-and bright-soliton Kerr combs in normal-dispersion resonators. *Phys. Rev. A* **2017**, *95*, 053863. [[CrossRef](#)]
47. Li, Z.; Xu, Y.; Todd, C.; Xu, G.; Coen, S.; Murdoch, S.G.; Erkintalo, M. Observations of existence and instability dynamics of near-zero-dispersion temporal Kerr cavity solitons. *Phys. Rev. Res.* **2021**, *3*, 043207. [[CrossRef](#)]
48. Godey, C.; Balakireva, I.V.; Coillet, A.; Chembo, Y.K. Stability analysis of the spatiotemporal Lugiato-Lefever model for Kerr optical frequency combs in the anomalous and normal dispersion regimes. *Phys. Rev. A* **2014**, *89*, 063814. [[CrossRef](#)]
49. Puzyrev, D.; Skryabin, D. Finesse and four-wave mixing in microresonators. *Phys. Rev. A* **2021**, *103*, 013508. [[CrossRef](#)]
50. Skryabin, D.; Fan, Z.; Villois, A.; Puzyrev, D. Threshold of complexity and Arnold tongues in Kerr-ring microresonators. *Phys. Rev. A* **2021**, *103*, L011502. [[CrossRef](#)]